Dieses Dokument ist eine Zweitveröffentlichung (Verlagsversion)

This is a self-archiving document (published version)

Jin-Jiang Zhang, Lin Yang, Fupin Liu et al.

Pushing Up the Size Limit of Boron-doped peri-Acenes : Modular Synthesis and Characterizations

Erstveröffentlichung in / First published in:

Angewandte Chemie. 2023, 62(48). Art-Nr. e202312055. Wiley-VCH. ISSN: 1521-3773

DOI: https://doi.org/10.1002/anie.202312055

Diese Version ist verfügbar / This version is available on:

https://nbn-resolving.org/urn:nbn:de:bsz:14-qucosa2-944110

Dieses Werk ist lizenziert unter einer Creative Commons Namensnennung 4.0 International Lizenz.
This work is licensed under a Creative Commons Attribution 4.0 International License.

SLUB
Wir führen Wissen.

TECHNISCHE UNIVERSITÄT DRESDEN

QUCOSA
Quality Content of Saxony

How to cite: *Angew. Chem. Int. Ed.* **2023**, *62*, e202312055
doi.org/10.1002/anie.202312055

Polycyclic Hydrocarbons

Pushing Up the Size Limit of Boron-doped *peri*-Acenes: Modular Synthesis and Characterizations

Jin-Jiang Zhang, Lin Yang, Fupin Liu, Gianluca Serra, Yubin Fu, Andrea Lucotti, Alexey A. Popov, Matteo Tommasini, Ji Ma, and Xinliang Feng**

Abstract: Heteroatom-doped *peri*-acenes (PAs) have recently attracted considerable attention considering their fascinating physical properties and chemical stability. However, the precise sole addition of boron atoms along the zigzag edges of PAs remains challenging, primarily due to the limited synthetic approach. Herein, we present a novel one-pot modular synthetic strategy toward unprecedented boron-doped PAs (B-PAs), including B-[4,2]PA (**1a-2**), B-[4,3]PA (**1b-2**) and B-[7,2]PA (**1c-3**) derivatives, through efficient intramolecular electrophilic borylation. Their chemical structures are unequivocally confirmed with a combination of mass spectrometry, NMR, and single-crystal X-ray diffraction analysis. Notably, **1b-2** exhibits an almost planar geometry, whereas **1a-2** displays a distinctive bowl-like distortion. Furthermore, the optoelectronic properties of this series of B-PAs are thoroughly investigated by UV/Vis absorption and fluorescence spectroscopy combined with DFT calculation. Compared with their parent all-carbon analogs, the obtained B-PAs exhibit high stability, wide energy gaps, and high photoluminescence quantum yields of up to 84%. This study reveals the exceptional ability of boron doping to finely tune the physicochemical properties of PAs, showcasing their potential applications in optoelectronics.

[n,m]*peri*-Acenes (PAs), which refers to 'm' rows of *peri*-fused [n]acenes,[1–2] have the intriguing characteristic of exhibiting a localized non-bonding π-state along the zigzag edges, making them potential candidates for organic spintronics (Figure 1a).[3–6] Additionally, PAs also serve as ideal finite model systems to investigate the electronic and magnetic properties of zigzag-edged graphene nanoribbons (GNRs).[7–8] However, the solution synthesis of large PAs is extremely challenging due to their intrinsic instability arising from the emerging open-shell character.[9–11] On the one hand, kinetic protection by introducing bulky groups along the zigzag edges of PAs has been developed to overcome this obstacle, affording the fairly stable PAs in solution,[12–15] such as the recently reported [4,2]PA,[16–18] [4,3]PA,[19] and the hitherto largest [7,2]PA.[20]

On the other hand, the introduction of heteroatoms along the zigzag edges of PAs has emerged as an alternative strategy to provide stable PA analogs (Figure 1b).[21] This approach could not only enhance the stability of the resulting systems but also be able to finely tailor their optoelectronic properties by varying the heteroatom type, doping position, and concentration. In 2015, Wagner et. al reported the synthesis of B-doped bisanthene (namely B-[3,2]PA, **I**) via Si/B exchange method.[22] In contrast to the unstable parent [3,2]PA toward molecular oxygen, **I** ex-

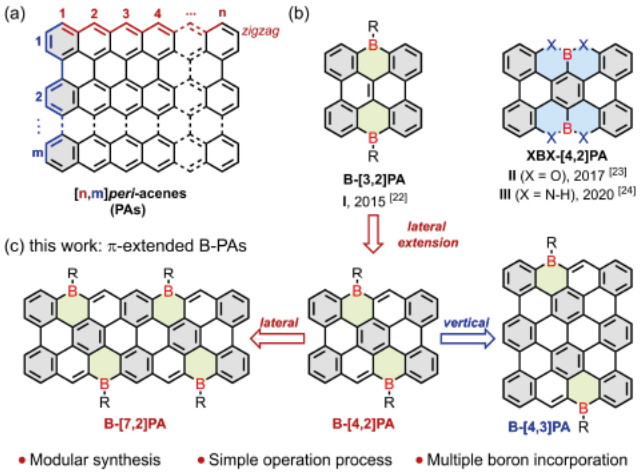

Figure 1. (a) Structure illustration of pristine [n,m]PAs; (b) Representative examples of heteroatom-doped [4,2]PAs; (c) Structures of bidirectional π-extended B-PAs in this work. The substituents are omitted for simplicity.

[*] J.-J. Zhang, Y. Fu, J. Ma, X. Feng
Max Planck Institute of Microstructure Physics
Weinberg 2, Halle, 06120 (Germany)
E-mail: ji.ma@mpi-halle.mpg.de
xinliang.feng@tu-dresden.de

L. Yang, J. Ma, X. Feng
Center for Advancing Electronics Dresden (cfaed) & Faculty of Chemistry and Food Chemistry, Technische Universität Dresden
Mommsenstrasse 4, 01062 Dresden, Germany

F. Liu, A. A. Popov
Leibniz Institute for Solid State and Materials Research (IFW) Dresden
Helmholtzstrasse 20, 01069 Dresden (Germany)

G. Serra, A. Lucotti, M. Tommasini
Dipartimento di Chimica, Materiali ed Ingegneria Chimica "G. Natta", Politecnico di Milano
Piazza Leonardo da Vinci 32, 20133 Milano (Italy)

© 2023 The Authors. Angewandte Chemie International Edition published by Wiley-VCH GmbH. This is an open access article under the terms of the Creative Commons Attribution License, which permits use, distribution and reproduction in any medium, provided the original work is properly cited.

© 2023 The Authors. Angewandte Chemie International Edition published by Wiley-VCH GmbH

hibited remarkable stability and intriguing optical properties, including the obvious blue-shifted maximum longest wavelength absorption (λ_{max} = 442 nm) and strong photoluminescence with high quantum yield (78 %) compared to that of parent non-emissive [3,2]PA (λ_{max} = 485 nm).[12] Despite the successful synthesis of **I**, the Si/B exchange strategy is not applicable for synthesizing large-sized B-PAs systems due to difficulties in obtaining the corresponding Si-containing precursors. So far, **I** stands as the only member of the B-PA family, and B-PAs larger in size than [3,2]PA remain elusive. To achieve the synthesis of extended B-PA analogs, a multi-heteroatom doping strategy has been developed, which relies on introducing other main group elements, such as oxygen (O) or nitrogen (N) into the zigzag edges of PAs alongside boron forming covalent bonds. In this respect, OBO-doped [4,2]PA (**II**) and NBN-doped [4,2]PA (**III**) were synthesized recently(Figure 1b).[23–24] The incorporation of OBO or NBN unit led to a largely increased HOMO–LUMO gap and intense photoluminescence compared to its kinetically stabilized analog [4,2]PA. Nevertheless, both OBO and NBN doping strategies significantly diminish the electronic conjugation of resultant systems. Therefore, the synthesis of diverse B-PAs larger than B-[3,2]PA (**I**) remains highly attractive to establish the fundamental correlation between their structure and optoelectronic properties.

Herein, we report an efficient one-pot synthetic method towards a series of B-PA derivatives (Figure 1c), including B-[4,2]PA (**1a-2**), B-[4,3]PA (**1b-2**), and B-[7,2]PA (**1c-3**), where the B-doped zigzag edges are formed via a sequence of lithiation, trans-metalation and electrophilic arene borylation from the iodine-containing precursors. The obtained B-PAs exhibit high stability under ambient conditions, enabling their full characterizations with high-resolution matrix-assisted laser desorption time-of-flight (HR MALDI-TOF) mass spectrometry and nuclear magnetic resonance (NMR) spectroscopy. Single-crystal X-ray analysis of **1a-2** and **1b-2** demonstrated that the boron atom locates at the zigzag edge and adopts trigonal planar geometry. Interestingly, **1a-2** displays a unique bowl-shaped geometry with bowl chirality, whereas **1b-2** exhibits a relatively planar structure. Moreover, the optoelectronic properties of resultant B-PAs are investigated by UV/Vis absorption spectroscopy and fluorescence spectroscopy together with DFT calculations. Compared with the kinetically stabilized PAs,[16,19] these B-PAs exhibit high stability with tunable energy gaps (1.79–2.39 eV). Notably, B-[4,2]PA (**1a-2**) shows an obvious bathochromic shift compared with its OBO/NBN-doped analogs (**II** and **III**),[23–24] demonstrating that the boron doping, where the hydroxy groups are installed at the boron sites, could not only furnish relatively stable PA analogs but also efficiently enhance the electronic conjugation of the resultant system. In contrast to non-emissive kinetically protected PAs and weak-emissive OBO/NBN-doped analogs, all the obtained B-PAs show intense fluorescence in their dichloromethane (DCM) solutions with high photoluminescence quantum yield of up to 84 % (**1b-2**). The developed approach in this work provides a straightforward strategy for introducing boron atoms into the zigzag edges of bidirectional π-extended PAs or even GNRs, which enables precise modification of their physicochemical properties.

The synthesis of **1a-2** was first carried out as shown in Scheme 1a. The precursor **2a** bearing two iodine atoms was prepared by a four-step reaction strategy according to the previous work.[16] Subsequently, **2a** was lithiated with *n*-butyllithium in its *o*-xylene solution at 0 °C, followed by trapping of the resulting aryllithium with boron tribromide (BBr_3), which was then heated to 150 °C for 16 hours to complete the intramolecular electrophilic borylation. At last, hydrolysis of the crude mixture with H_2O at room temperature successfully furnished partially borylated product **1a-1** and fully borylated target **1a-2** in 48 % and 32 % yield, respectively. Furthermore, the hydroxyl group in **1a-1** could be replaced by mesityl ring, giving **1a-Mes** with a yield of 35 %. During our attempts to convert **1a-2** into its corresponding mesityl-substituted compound, we successfully detected the desired product through mass analysis of the crude mixture. However, isolating the target compound has proven to be quite challenging, potentially attributable to its low stability under ambient conditions resulting from its low LUMO energy level (−2.46 eV) (Figures S2).[25] To further demonstrate the applicability of this one-pot ap-

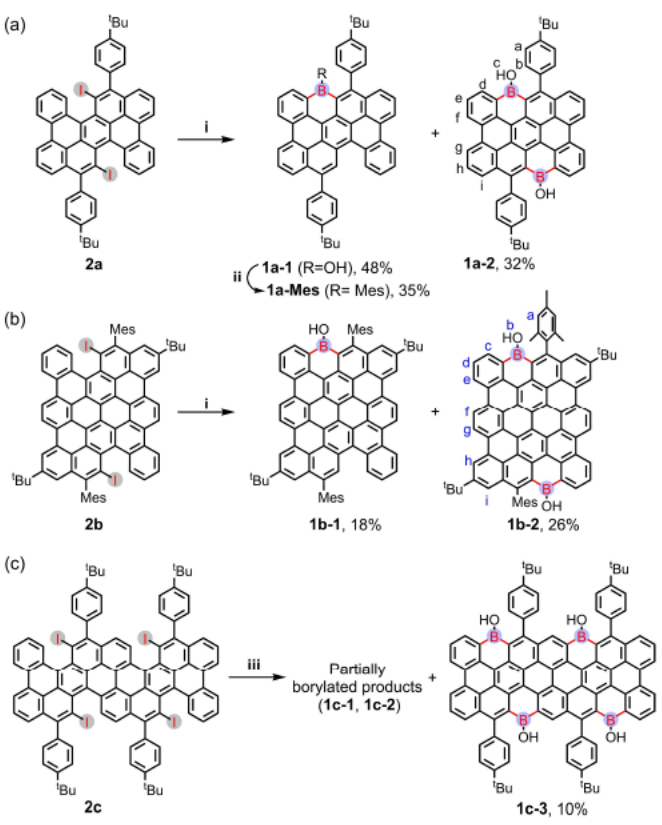

Scheme 1. Synthetic routes towards B-PA derivatives, including (a) B-[4,2]PA (**1a-2**), (b) B-[4,3]PA (**1b-2**) and (c) B-[7,2]PA (**1c-3**). Regents and conditions: (i) 1. *n*-BuLi (4 eq), *o*-xylene, 0 °C; 2. BBr_3 (10.0 eq), 150 °C; 3. hydrolysis. (ii) 1. BBr_3, toluene, 110 °C; 2. MesMgBr, rt. (iii) 1. *n*-BuLi (8.0 eq), 4-*tert*-butylbenzene, 0 °C; 2. BBr_3 (excess), 165 °C; 3. hydrolysis.

© 2023 The Authors. Angewandte Chemie International Edition published by Wiley-VCH GmbH

15213773, 2023, 48, Downloaded from https://onlinelibrary.wiley.com/doi/10.1002/anie.202312055 by Saechsische Landesbibliothek, Wiley Online Library on [24/06/2024]. See the Terms and Conditions (https://onlinelibrary.wiley.com/terms-and-conditions) on Wiley Online Library for rules of use; OA articles are governed by the applicable Creative Commons License

proach, we aimed to synthesize the larger B-[4,3]PA (**1b-2**) and B-[7,2]PA (**1c-3**) derivatives, which represent vertical and lateral extensions of B-[4,2]PA (**1a-2**), respectively. Precursors **2b** and **2c** were obtained following the reported procedures,[19–20] respectively. Satisfactorily, the treatment of **2b** under the same reaction condition used for synthesizing **1a-2** successfully gave the desired dual-B-[4,3]PA derivative (**1b-2**) in 26% yield, along with the formation of the partially borylated compound **1b-1** in 18% yield (Scheme 1b). Nevertheless, the reaction efficiency was dramatically inhibited when **2c** was subjected to this standard condition. The low reaction efficiency together with complicated byproducts made the isolation of the targeted B-[7,2]PA difficult. After carefully optimizing the reaction conditions, the reaction efficiency could be smoothly promoted by elevating the reaction temperature (oil bath: 165 °C) and increasing the loading of BBr_3 (using excess). These adjustments enabled the successful isolation of B-[7,2]PA (**1c-3**) along with the partially borylated byproducts dual-B-[7,2]PA (**1c-1**) and tri-B-[7,2]PA (**1c-2**) (Scheme 1c and Figures S8–10).

The chemical identities of the obtained B-PAs (**1a-2**, **1b-2** and **1c-3**) were first confirmed by HR MALDI-TOF mass spectrometry. In their respective mass spectrum, only one dominant mass peak, $m/z = 742.3216$ for **1a-2**, 1046.4460 for **1b-2**, and 1330.5649 for **1c-3**, was observed, respectively, which is in good agreement with its expected molecular mass and isotopic distribution (Figure 2a–d). Compound **1a-2** exhibited limited solubility in dichloromethane (DCM), tetrahydrofuran (THF), and even in dimethyl sulfoxide (DMSO). As a result, its ^{1}H NMR spectrum could only be recorded in $C_2D_2Cl_4$ at high temperatures (353 K). Thanks to the good solubility of **1b-2** in common organic solvents like DCM, its ^{1}H NMR spectroscopy was readily recorded in CD_2Cl_2 at room temperature. As shown in Figures 2e and 2f, both **1a-2** and **1b-2** displayed well-resolved proton signals, which are readily assigned by a combination of different 2D NMR techniques. The proton signals of f and g in **1a-2**, as well as e, f, g, and h in **1b-2** displayed pronounced downfield chemical shifts due to the deshielding effects induced by steric hindrance at the bay regions. In addition, the proton of hydroxide group (peak b) in **1b-2** presented a downfield chemical shift compared with that (peak c) of **1a-2**, which could be ascribed to the influence of the adjacent bulky mesityl ring. However, the poor solubility of **1c-3** posed a challenge in fully characterizing it by NMR. Therefore, the validation of the structure of **1c-3** was further carried out using IR and Raman spectroscopy in conjunction with theoretical simulations (For detailed information, refer to section 8 in the Supporting Information).

The structures of **1a-1**, **1a-2** and **1b-2** were unequivocally confirmed by X-ray crystallographic analysis, in which the single crystals were obtained by slow evaporation of their DCM solution at room temperature, respectively.[26] It is shown that partially borylated [4,2]PA (**1a-1**) exhibits nonplanar geometry due to the existence of [4]helicene subunit, and the torsional angle is 25.49° (Figure 3a). For fully borylated compound **1a-2**, it displays bowl-like geometry with a bowl depth of 0.696 Å that is defined with the perpendicular distance from the center of the benzene ring to the parallel planes containing the eight periphery carbon atoms of armchair edges (Figure 3b and 3e). In contrast to **1a-2**, its vertical extended analog (**1b-2**) shows almost-perfect planar geometry (Figure 3c). The C–B bonds length in **1a-1**, **1a-2** and **1b-2** are in the range of 1.536(4)-1.561(5) Å, which are comparable with similar reported cases.[27–28] In their solid states, the unit cell of **1a-1** contains

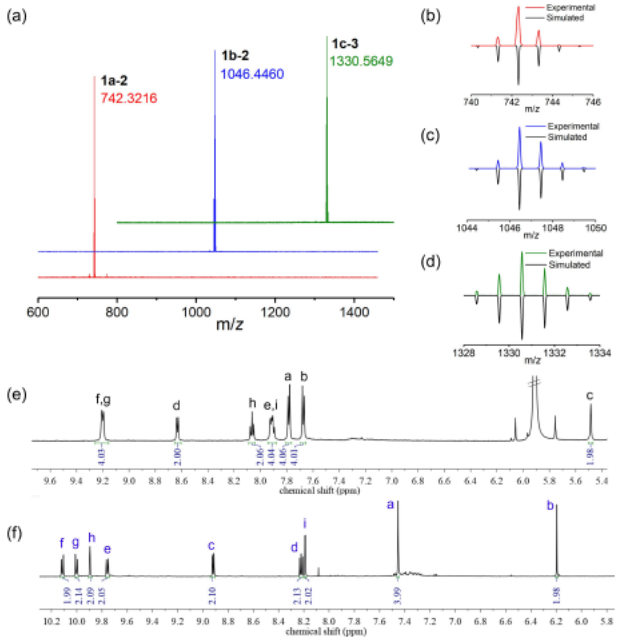

Figure 2. (a) HR MALDI-TOF mass spectra of **1a-2** (red), **1b-2** (blue) and **1c-3** (green); (b–d) Comparisons of measured and simulated isotopic distribution patterns of **1a-2** (b), **1b-2** (c) and **1c-3** (d); Partial ^{1}H NMR spectra of (e) **1a-2** (600 MHz, 353 K, $C_2D_2Cl_4$) and (f) **1b-2** (600 MHz, 298 K, CD_2Cl_2). For full spectra see Supporting Information. Peak assignments are according to those of the molecular structures in Scheme 1.

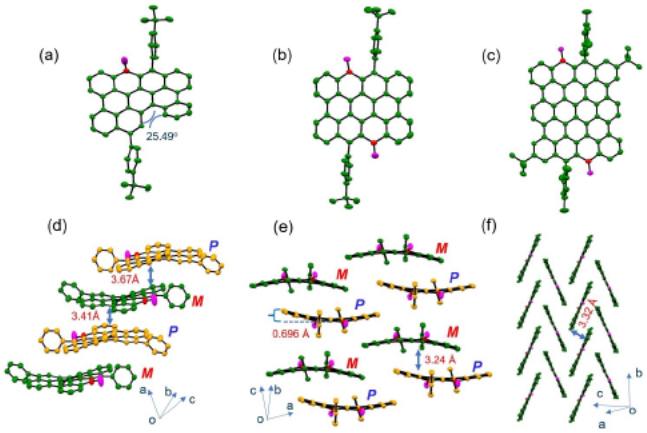

Figure 3. X-ray crystallographic molecular structures of **1a-1** (a), **1a-2** (b) and **1b-2** (c) (C: green, B: red, O: purple. H atoms are omitted for clarity) as well as the packing arrangements of **1a-1** (d), **1a-2** (e), and **1b-2** (f) (*tert*-butyl and mesityl group are omitted for clarity).

© 2023 The Authors. Angewandte Chemie International Edition published by Wiley-VCH GmbH

15213773, 2023, 48, Downloaded from https://onlinelibrary.wiley.com/doi/10.1002/anie.202312055 by Saechsische Landesbibliothek, Wiley Online Library on [24/06/2024]. See the Terms and Conditions (https://onlinelibrary.wiley.com/terms-and-conditions) on Wiley Online Library for rules of use; OA articles are governed by the applicable Creative Commons License

two enantiomers with helical chirality (*M*: green color; *P*: orange color) and they pack into an ordered head-to-tail columnar arrangement along the *c*-axis, where the distances between two enantiomers are in the range of 3.41 to 3.67 Å (Figure 3d). Interestingly, **1a-2** displays unique bowl chirality due to its reflection asymmetric feature and the steric repulsion caused by the substituents along the zigzag edges.[29–32] To the best of our knowledge, this is the first example of tricoordinate B-doped polycyclic aromatic hydrocarbons (PAHs) with bowl chirality (Figure 3e). In the crystal packing, two enantiomers (*M* and *P*) of **1a-2** form the face-to-face π-stacked dimer structure in its unit cell with a distance of 3.24 Å, and the unit cell is further arranged into an ordered columnar superstructure. In contrast to **1a-2**, the packing diagram of **1b-2** is best described by a herringbone stacked structure, where the average distance between two parallel planes is 3.32 Å (Figure 3f).

To elucidate the relationship between their structures and optical properties, we recorded the UV/Vis absorption and fluorescence emission of compounds **1a-1**, **1a-2**, **1a-Mes**, **1b-2** and **1c-3** in anhydrous DCM solution (Figure 4). The lowest energy absorption maxima (λ_{max}) for this series of B-PAs fall in the visible region spanning from 497 nm (**1a-2**) to 643 nm (**1c-3**). Time-dependent density functional theory (TD-DFT) calculations reveal that the lowest energy absorption bands of those compounds are assignable to their S_0–S_1 (HOMO–LUMO) transition, with reasonable oscillator strengths ranging from 0.5 to 1.14 (see details in the Supporting Information). Compared with the λ_{max} of **1a-2** at 497 nm, **1b-2** shows an obvious bathochromic shift (44 nm) with λ_{max} = 541 nm due to its vertically extended π-conjugation (Figure 4a). In addition, the absorption maximum reveals a further redshift from 541 to 643 nm when the π-conjugation is laterally extended from **1b-2** to B-[7,2]PA derivative (**1c-3**). Compared with OBO/NBN-doped [4,2]PAs **II** (λ_{max} = 430 nm) and **III** (λ_{max} = 485 nm), the longest wavelength absorption maxima of **1a-2** exhibits a noticeable redshift, which suggests the enhanced electron conjugation in **1a-2**. Noteworthily, by replacing the hydroxyl group on the boron atom with the mesityl group, the maximum longest absorption peak displays an obvious redshift from 499 nm (**1a-1**) to 544 nm (**1a-Mes**), suggesting the significant influence of substituent at the boron site on modifying the optoelectronic properties. The optical energy gaps of **1a-2**, **1b-2** and **1c-3**, deduced from their absorption onsets, are 2.39, 2.24 and 1.79 eV, respectively. Furthermore, fluorescence spectra show that the emission band maxima of those compounds fall in the range between 510 (**1a-2**) and 653 nm (**1c-3**) (Figure 4b). Similarly, the emission wavelength also shows a redshift upon increasing the conjugation length from **1a-2** to **1c-3** or replacing hydroxyl substituent (**1a-1**) with the mesityl group (**1a-Mes**). Besides, **1a-2**, **1b-2** and **1c-3** show a rather small Stokes shift of 13, 3 and 9 nm, respectively, due to the rigid molecular scaffold. In stark contrast with non-emissive kinetically protected PAs[16–17,19–20] and weak emissive OBO/NBN-doped cases (**II** and **III**) (Figure 1a), all the obtained compounds in this work exhibit strong fluorescence in its DCM solution upon excitation. Among them, **1b-2** shows the highest photoluminescence (PL) quantum yields (Φ_{PL}) of 84 % due to the most stiffness of the backbone in combination with a low tendency of self-aggregation. These results demonstrated the superiority of boron doping at the molecular backbone in modulating the optical properties of PA systems.

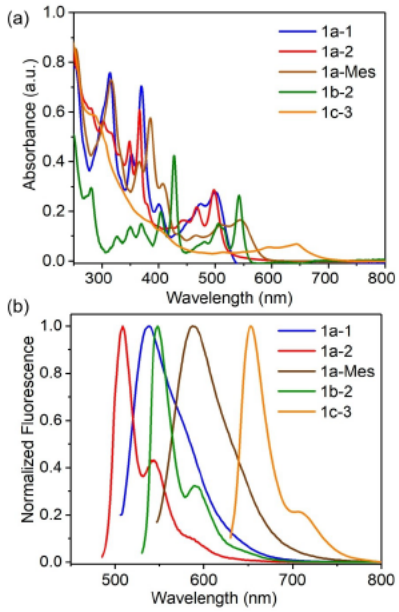

Figure 4. UV/Vis absorption (a) and fluorescence (b) spectra of the obtained B-PAs from **1a-1** to **1c-3** (10^{-6} M in CH_2Cl_2, 298 K).

To gain insight into the influence of boron doping on the electronic properties of PAs, DFT calculations are performed at the B3LYP/6-31G(d) level for **1a-2**, **1b-2** and **1c-3**. As shown in Figure 5a, although the HOMO and LUMO are distributed over the entire molecule, the *p*-orbital of boron makes a significant contribution to their LUMO. From **1a-2** to **1c-3**, the energy level of HOMO gradually increases from −4.93 to −4.62 eV. The LUMO energy level of **1a-2** (−2.15 eV) and **1b-2** (−2.19 eV) display a slight change, whereas that of **1c-3** significantly decreases to −2.50 eV due to the higher boron doping concentration (Figure 5a). The calculated energy gap of **1a-2** is 2.78 eV, which is higher by 1.02 eV than that of pristine carbon-based [4,2]PA (Figure 5b). Compared with OBO- and NBN-[4,2]PA (**II** and **III**), the calculated energy gap of **1a-2** significantly decreased by 0.79 and 0.59 eV, respectively, due to the enhanced conjugated structure, which in agreement with the experimental optical energy gap. In addition, the local aromaticity of **1a-2**, **1b-2** and **1c-3** was also assessed by using anisotropy of the induced current density (ACID) and the nucleus-independent chemical shifts (NICS) calculations. ACID plots of **1a-2**, as a representative example, reveal that the continuous current flow in the whole molecular backbone is blocked by the six-membered boracycle (Figure 5c, for **1b-2** and **1c-3**, see Figure S20), indicating that the boron-embedded six-membered rings display anti-aromatic character. This result is further supported by the positive NICS(1) value (+2.89 ppm) of boron-containing ring B in **1a-2**, which is in stark contrast with that of pristine [4,2]PA,

© 2023 The Authors. Angewandte Chemie International Edition published by Wiley-VCH GmbH

15213773, 2023, 48, Downloaded from https://onlinelibrary.wiley.com/doi/10.1002/anie.202312055 by Saechsische Landesbibliothek, Wiley Online Library on [24/06/2024]. See the Terms and Conditions (https://onlinelibrary.wiley.com/terms-and-conditions) on Wiley Online Library for rules of use; OA articles are governed by the applicable Creative Commons License

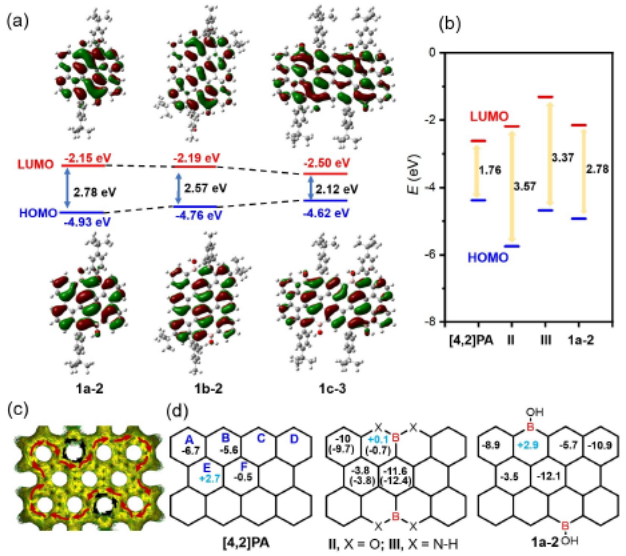

Figure 5. (a) Calculated (B3LYP/6-31G(d)) molecular orbitals and energy diagrams of **1a-2**, **1b-2** and **1c-3**; (b) Calculated energy level of compounds **[4,2]PA**, **II**, **III** and **1a-2**; (c) ACID plots of **1a-2** (red circle: aromatic ring; black circle: anti-aromatic ring); (d) NICS(1) of **[4,2]PA**, **II**, **III** (values in the parentheses) and **1a-2** calculated at the GIAO B3LYP/6-311+G(2d,p) level.

II and **III** with either aromaticity or non-aromaticity feature (Figure 5d). Notably, rings A and F in **1a-2** (−8.9 and −12.1 ppm) are more aromatic compared with that of pristine [4,2]PA (−6.7 and −0.5 ppm). Differently, ring E in **1a-2** exhibits moderate aromaticity, whereas it displays moderate antiaromatic feature in pristine [4,2]PA. These results manifest that the significant influence of boron doping on tuning the electronic properties of PAs.

In conclusion, we have successfully synthesized a novel class of bench-stable B-PAs, including B-[4,2]PA(**1a-2**), B-[4,3]PA (**1b-2**) and B-[7,2]PA (**1c-3**) derivatives by intramolecular tandem electrophilic borylation from iodine-containing precursors. NMR spectroscopy and single-crystal X-ray diffraction analysis of **1a-1**, **1a-2** and **1b-2** unambiguously elucidated their chemical structures. Interestingly, **1a-2** displayed unique bowl chirality that has never been observed for tri-coordinate B-PAHs. The significant influence of sole boron doping at zigzag edges of PAs was unveiled, establishing a clear correlation between their structure and physicochemical properties. Specifically, compared with kinetically protected PA analogs, the resultant B-PAs exhibited intensive fluorescence with high quantum yield, wider energy gap as well as different frontier orbitals configuration and local aromaticity. Our study significantly enriches the scope of the [n,m]PA family and B-doped PAHs, rendering them attractive candidates for the future development of organic electronics applications.

Acknowledgements

This research was financially supported by the EU Graphene Flagship (Graphene Core 3, 881603), ERC Consolidator Grant (T2DCP, 819698), H2020-MSCA-ITN (ULTIMATE, No. 813036), the Center for Advancing Electronics Dresden (cfaed), H2020-EU.1.2.2.—FET Proactive Grant (LIGHT-CAP, 101017821) and the DFG-SNSF Joint Switzerland-German Research Project (EnhanTopo, No. 429265950). The authors acknowledge the use of computational facilities at the Center for information services and high performance computing (ZIH) at TU Dresden. Diffraction data have been collected on BL14.2 at the BESSY II electron storage ring operated by the Helmholtz-Zentrum Berlin, and we appreciate the help of Manfred Weiss and his team during the experiments at BESSY II. We also thank Dr. Tilo Lübken (Organic Chemistry, Technische Universität Dresden) for 2D NMR analysis. Open Access funding enabled and organized by Projekt DEAL.

Conflict of Interest

The authors declare no conflict of interest.

Data Availability Statement

The data that support the findings of this study are available from the corresponding author upon reasonable request.

Keywords: Boron Doping · Electrophilic Borylation · Peri-Acenes · Polycyclic Aromatic Hydrocarbon · π-Extension

[1] Z. Sun, Q. Ye, C. Chi, J. Wu, *Chem. Soc. Rev.* **2012**, *41*, 7857–7889.
[2] A. Konishi, T. Kubo, *Physical Organic Chemistry of Quinodimethanes*, Springer, Berlin **2017**, pp. 69–105.
[3] D.-e. Jiang, B. G. Sumpter, S. Dai, *J. Chem. Phys.* **2007**, *127*, 124703.
[4] D.-e. Jiang, S. Dai, *Chem. Phys. Lett.* **2008**, *466*, 72–75.
[5] F. Moscardó, E. San-Fabián, *Chem. Phys. Lett.* **2009**, *480*, 26–30.
[6] F. Plasser, H. Pašalić, M. H. Gerzabek, F. Libisch, R. Reiter, J. Burgdörfer, T. Müller, R. Shepard, H. Lischka, *Angew. Chem. Int. Ed.* **2013**, *52*, 2581–2584.
[7] P. Ruffieux, S. Wang, B. Yang, C. Sánchez-Sánchez, J. Liu, T. Dienel, L. Talirz, P. Shinde, C. A. Pignedoli, D. Passerone, *Nature* **2016**, *531*, 489–492.
[8] O. Hod, V. Barone, G. E. Scuseria, *Phys. Rev. B* **2008**, *77*, 035411.
[9] M. Bendikov, H. M. Duong, K. Starkey, K. N. Houk, E. A. Carter, F. Wudl, *J. Am. Chem. Soc.* **2004**, *126*, 7416–7417.
[10] M. C. dos Santos, *Phys. Rev. B* **2006**, *74*, 045426.
[11] E. Clar, *The Aromatic Sextet*, Wiley, London **1972**.
[12] A. Konishi, Y. Hirao, M. Nakano, A. Shimizu, E. Botek, B. Champagne, D. Shiomi, K. Sato, T. Takui, K. Matsumoto, *J. Am. Chem. Soc.* **2010**, *132*, 11021–11023.
[13] A. Konishi, Y. Hirao, K. Matsumoto, H. Kurata, R. Kishi, Y. Shigeta, M. Nakano, K. Tokunaga, K. Kamada, T. Kubo, *J. Am. Chem. Soc.* **2013**, *135*, 1430–1437.
[14] J. Liu, P. Ravat, M. Wagner, M. Baumgarten, X. Feng, K. Müllen, *Angew. Chem. Int. Ed.* **2015**, *54*, 12442–12446.
[15] M. Mamada, R. Nakamura, C. Adachi, *Chem. Sci.* **2021**, *12*, 552–558.

© 2023 The Authors. Angewandte Chemie International Edition published by Wiley-VCH GmbH

15213773, 2023, 48, Downloaded from https://onlinelibrary.wiley.com/doi/10.1002/anie.202312055 by Saechsische Landesbibliothek, Wiley Online Library on [24/06/2024]. See the Terms and Conditions (https://onlinelibrary.wiley.com/terms-and-conditions) on Wiley Online Library for rules of use; OA articles are governed by the applicable Creative Commons License

[16] M. R. Ajayakumar, Y. Fu, J. Ma, F. Hennersdorf, H. Komber, J. J. Weigand, A. Alfonsov, A. A. Popov, R. Berger, J. Liu, K. Müllen, X. Feng, *J. Am. Chem. Soc.* **2018**, *140*, 6240–6244.
[17] Y. Ni, T. Y. Gopalakrishna, H. Phan, T. S. Herng, S. Wu, Y. Han, J. Ding, J. Wu, *Angew. Chem. Int. Ed.* **2018**, *57*, 9697–9701.
[18] S. Mishra, T. G. Lohr, C. A. Pignedoli, J. Liu, R. Berger, J. I. Urgel, K. Müllen, X. Feng, P. Ruffieux, R. Fasel, *ACS Nano* **2018**, *12*, 11917–11927.
[19] J. J. Shen, Y. Han, S. Dong, H. Phan, T. S. Herng, T. Xu, J. Ding, C. Chi, *Angew. Chem. Int. Ed.* **2021**, *60*, 4464–4469.
[20] M. R. Ajayakumar, J. Ma, A. Lucotti, K. S. Schellhammer, G. Serra, E. Dmitrieva, M. Rosenkranz, H. Komber, J. Liu, F. Ortmann, M. Tommasini, X. Feng, *Angew. Chem. Int. Ed.* **2021**, *60*, 13853–13858.
[21] X. Y. Wang, X. Yao, A. Narita, K. Müllen, *Acc. Chem. Res.* **2019**, *52*, 2491–2505.
[22] V. M. Hertz, M. Bolte, H. W. Lerner, M. Wagner, *Angew. Chem. Int. Ed.* **2015**, *54*, 8800–8804.
[23] X. Y. Wang, A. Narita, W. Zhang, X. Feng, K. Müllen, *J. Am. Chem. Soc.* **2016**, *138*, 9021–9024.
[24] Y. Fu, X. Chang, H. Yang, E. Dmitrieva, Y. Gao, J. Ma, L. Huang, J. Liu, H. Lu, Z. Cheng, S. Du, H. J. Gao, X. Feng, *Angew. Chem. Int. Ed.* **2021**, *60*, 26115–26121.
[25] K. Liu, R. A. Lalancette, F. Jakle, *J. Am. Chem. Soc.* **2017**, *139*, 18170–18173.
[26] Deposition numbers 2286278 (**1a-1**), 2286279 (**1a-2**) and 2286280 (**1b-2**) contain the supplementary crystallographic data for this paper. These data are provided free of charge by the joint Cambridge Crystallographic Data Centre and Fachinformationszentrum Karlsruhe Access Structures service.
[27] R. J. Kahan, D. L. Crossley, J. Cid, J. E. Radcliffe, M. J. Ingleson, *Angew. Chem. Int. Ed.* **2018**, *57*, 8084–8088.
[28] J. M. Farrell, C. Mutzel, D. Bialas, M. Rudolf, K. Menekse, A. M. Krause, M. Stolte, F. Würthner, *J. Am. Chem. Soc.* **2019**, *141*, 9096–9104.
[29] K. Kise, S. Ooi, H. Saito, H. Yorimitsu, A. Osuka, T. Tanaka, *Angew. Chem. Int. Ed.* **2022**, *61*, e202112589.
[30] Y. Wang, O. Allemann, T. S. Balaban, N. Vanthuyne, A. Linden, K. K. Baldridge, J. S. Siegel, *Angew. Chem. Int. Ed.* **2018**, *57*, 6470–6474.
[31] M. A. Petrukhina, K. W. Andreini, L. Peng, L. T. Scott, *Angew. Chem. Int. Ed.* **2004**, *43*, 5477–5481.
[32] J. Wu, G. Zhang, *Angew. Chem. Int. Ed.* **2022**, *61*, e202208061.

Manuscript received: August 17, 2023
Accepted manuscript online: October 12, 2023
Version of record online: October 27, 2023

© 2023 The Authors. Angewandte Chemie International Edition published by Wiley-VCH GmbH

15213773, 2023, 48, Downloaded from https://onlinelibrary.wiley.com/doi/10.1002/anie.202312055 by Saechsische Landesbibliothek, Wiley Online Library on [24/06/2024]. See the Terms and Conditions (https://onlinelibrary.wiley.com/terms-and-conditions) on Wiley Online Library for rules of use; OA articles are governed by the applicable Creative Commons License